Proceedings of the ASME 2010 3rd Joint US-European Fluids Engineering Summer Meeting and 8th International Conference on Nanochannels, Microchannels, and Minichannels
FEDSM-ICNMM2010
August 1-5, 2010, Montreal, Canada

FEDSM-ICNMM2010-30356

INFLUENCE OF WALL PROXIMITY AND FREE SURFACE ON WAKE OF TWO SIDE-BY-SIDE CIRCULAR CYLINDERS: PIV MEASUREMENT AND POD ANALYSIS

S.S. Paul
Department of Mechanical and Manufacturing Engineering, University of Manitoba,
Winnipeg, MB, R3T 5V6, Canada

ABSTRACT

The paper reports on an experimental study of turbulent flow around a pair of circular cylinders with a pitch ratio of two. The cylinders were located in the vicinity of a plane wall, in a uniform stream, and adjacent to a free surface in an open channel. The Reynolds number based on depth of flow and fresstream velocity was 30300 while the Froude number was 0.3. A particle image velocimetry technique was used to conduct detailed velocity measurements around and in the near wake region of the cylinder pairs, from which contours and profiles of the mean velocities and turbulent statistics were obtained and discussed. The proper orthogonal decomposition was then applied to provide an insight into the structure of the flow. Reconstruction of the fluctuating velocity components for various numbers of modes were also shown to investigate the role of large-scale structures.

NOMENCLATURE

D	cylinder diameter [m]
L_r	recirculation length [m]
T	cylinder centre-to-centre spacing [m]
Re	Reynolds number (= $U_\infty D/\nu$)
U	x-direction mean velocity component [m/s]
U_∞	approach velocity [m/s]
u	x-direction velocity fluctuation [m/s]
$-uv$	Reynolds shear stress [m^2/s^2]
V	y-direction mean velocity component [m/s]
v	y-direction velocity fluctuation [m/s]
x	streamwise coordinate [m]
y	transverse coordinate [m]

Greek Symbols

$\phi^{(i)}$	Eigenfunction of mode i
$\lambda^{(i)}$	Eigenvalue of mode i
ρ	fluid density [kg/m^3]
ν	kinematic viscosity [m^2/s]

INTRODUCTION

Flow past a cylinder located in the vicinity of a plane boundary or close to a free surface has a potential relevance to a large number of practical engineering applications, such as pipelines on seabed, underwater cables, and submarines. The structure of this type of flow is more complex than those found around cylinders in a uniform stream [1]. For example, the no-slip boundary condition imposed by the plane wall and the associated velocity gradient produce intense vortical structures that interact with the vortices shed from the cylinders. The effect of proximity of a plane wall on the flow around a single cylinder has been experimentally and numerically investigated by many researchers. Extensive reviews and discussion can be found in Bearman and Zdravkovich [2], Price et al. [1], and Dipankar and Sengupta [3]. The related problem of flow past a cylinder submerged at various depths beneath a free surface also provides a useful point of reference for the current study. Excellent review articles on flow close to a free surface have been presented, for example, by Sheridan et al. [4] and Reichl et al. [5]. Sheridan et al. [4] investigated the wake characteristics at various depths beneath the free-surface. They found that the jet of fluid passing over the cylinder exhibits the following states: attachment to the free surface; attachment to the cylinder; and an intermediate state in-between. Reichl et al. [5] performed numerical simulation to study the flow around a cylinder close to a free surface at a Reynolds number of 180, Froude number range of 0.0 to 0.7, and for gap ratio between 0.1 and 5.0. They observed that the flow is largely governed by geometrical constraints in the low-Froude-number limit. Flow visualization study of the interaction between cylinder wake and the free surface is provided by Lee and Daichin [6].

In contrast to the considerable attention that has been devoted to flow around cylinder pairs in uniform stream, study on the structure of flow past two side-by-side circular cylinders in the vicinity of plane wall and adjacent to a free surface has received relatively little attention. Detailed reviews and discussions on flow around two identical circular cylinders in a uniform stream can be found in Sumner et al. [7] and Wang and Zhou [8]. Sumner et al. [7] used a particle image velocimetry (PIV) system to study the flow around two side-by-side circular cylinders at Reynolds numbers that range from 500 to 3000 and $1 \le T/D \le 5$ (where T/D is pitch ratio; see Figure 1). They observed three vortex shedding patterns: a single bluff body pattern for $1 \le T/D \le 1.2$, a deflected pattern for $1.2 \le T/D \le 2.2$, and anti-phase and in-phase synchronized patterns for $2.2 \le T/D \le 4.5$. The predominance of anti-phase vortex shedding for $T/D > 2$ was verified by Sumner et al. [7]. Wang and Zhou [8] used flow visualization, PIV, and hot-wire measurements to study the vortex generation, interaction and downstream evolution of two side-by-side circular cylinders for the Reynolds number range of 120 to 1100 and the dimensionless spacing was varied from $T/D = 1.2$ to 2.0. It was found that the flow structure and its downstream evolution are closely linked to the phase relationship between the gap vortex in the wide and narrow wakes.

Proper orthogonal decomposition (POD) has emerged as a powerful statistical technique for extracting dominant features and identifying coherent structures. POD was first introduced in turbulence research by Lumley [9]. Lumley defined organized motions (*i.e.*, coherent structures) embedded in turbulent flow as the structure,ϕ with the largest mean-square projection onto the velocity field. In principle, the POD analysis consists of finding a series of eigenfunctions or POD modes, ϕ^n, with associated turbulent kinetic energy in the n^{th} mode, λ^n, from a data set. The velocity field can then be expressed as a linear combination of its eigenfunctions (Hammad and Milanovic [10]). POD captures the most energetic and hence largest structures of the flow in the first modes. Detailed reviews and applications of POD can be found, for example, in Berkooz et al. [11], Holmes et al. [12], and Delville et al. [13]. The structure identification based on the POD has been implemented in various types of flows such as jets, backward facing step, and cylinder wakes. The POD analysis requires the knowledge of two-point spatial correlation function. Hence, would require the use of multi-point measurement techniques such as rakes of hot-wires and PIV. Since the PIV is a non-intrusive whole-field measurement technique, it is well suited for POD analysis.

In the present study, a combination of the PIV and POD is employed to investigate flow structures in the near-wake of two side-by-side circular cylinders located in the vicinity of plane wall, uniform stream, and adjacent to a free surface in an open channel. This is achieved by performing detailed velocity measurements in the near-wake of the cylinder pairs. The measurements were conducted using a particle image velocimetry. From the PIV data, the mean velocities and one-point turbulent statistics were obtained. The proper orthogonal decomposition is then applied to analyze the PIV data, and to extract the large scale structures so that their dynamic roles can be studied.

POD ANALYSIS

The method of snapshots proposed by Sirovich [14] was employed to perform a POD analysis of the measured velocity field. By this method, each instantaneous PIV vector map is considered a snapshot of the flow, and the total number of vectors in each snapshot is designated by M while the total number of snapshots is denoted by N. The snapshot method is computationally more efficient than the direct method when $M >> N$ as in the present PIV experiment. The streamwise (u) and transverse (v) components of the fluctuating velocity (u_j^n, v_j^n) are obtained by subtracting the ensemble averaged snapshot ($\overline{\boldsymbol{u}}$) from each snapshot ($\hat{\boldsymbol{u}}^{\boldsymbol{n}}$), where the index n runs through the N snapshots and j runs through the M positions of velocity vectors in a given snapshot (*i.e.* $u_j = u(x_j, y_j)$). The fluctuating velocity components from the N snapshots are then arranged in a matrix $\boldsymbol{U}$ as:

$$\boldsymbol{U} = \begin{bmatrix} \boldsymbol{u}^1 & \boldsymbol{u}^2 & \cdots & \boldsymbol{u}^N \end{bmatrix} = \begin{bmatrix} u_1^1 & u_1^2 & \cdots & u_1^N \\ \vdots & \vdots & \vdots & \vdots \\ u_M^1 & u_M^2 & \cdots & u_M^N \\ v_1^1 & v_1^1 & \cdots & v_1^1 \\ \vdots & \vdots & \vdots & \vdots \\ v_M^1 & v_M^2 & \cdots & v_M^2 \end{bmatrix} \quad (1)$$

The $N \times N$ auto-covariance matrix $\boldsymbol{C}$ is obtained from:

$$\boldsymbol{C} = \boldsymbol{U}^T \boldsymbol{U} \quad (2)$$

A set of N eigenvalues, $\boldsymbol{\lambda^i}$, and a corresponding set of orthonormal eigenvectors, $\boldsymbol{A}^i$ which satisfy:

$$\boldsymbol{C}\boldsymbol{A}^i = \boldsymbol{\lambda}^i \boldsymbol{A}^i \quad (3)$$

can be evaluated from the auto-covariance matrix; where i runs from 1 to N. The eigenvalues are ordered by decreasing value as follows:

$$\boldsymbol{\lambda}^1 > \boldsymbol{\lambda}^2 \cdots\cdots > \boldsymbol{\lambda}^N > 0 \quad (4)$$

The normalized POD modes ($\boldsymbol{\phi^i}$) are constructed from the projection of the eigenvectors ($\boldsymbol{A}^i$) on to the original fields as follows:

$$\boldsymbol{\phi}^i = \frac{\sum_{n=1}^{N} A_n^i \boldsymbol{u}^n}{\left\| \sum_{n=1}^{N} A_n^i \boldsymbol{u}^n \right\|}, \qquad \boldsymbol{i} = 1, \ldots, \boldsymbol{N} \tag{5}$$

where A_n^i is the nth component of the eigenvector corresponding to λ^i. Here $\|.\|$ is the L_2-norm. The POD coefficients, a_i of each mode were calculated by projecting the fluctuating part of the velocity field onto the calculated POD modes as follows:

$$\boldsymbol{a}^n = \boldsymbol{\Psi}^T \boldsymbol{u}^n \tag{6}$$

where, $\boldsymbol{\Psi} = [\boldsymbol{\phi}^1\ \boldsymbol{\phi}^2\ \ldots\ \boldsymbol{\phi}^N]$. The expansion of any member of the ensemble using an arbitrary number of modes m was performed using:

$$\tilde{\boldsymbol{u}}^n = \sum_{i=1}^{m} \boldsymbol{a}_i^n \boldsymbol{\phi}^i = \boldsymbol{\psi a}^n \tag{7}$$

Equation 7 is known as the proper orthogonal decomposition of u^n; it gives the best approximation of the data ensemble u^n in the sense that the average least-squares truncation error is a minimum for any given number $m \leq N$ of basis functions over all possible sets of orthogonal basis functions.

The total energy, E of the flow field in the ensemble is equal to the sum of all the eigenvalues given by:

$$E = \sum_{i=1}^{N} \lambda_i \tag{8}$$

Moreover, the energy fraction associated with the i^{th} mode is given by:

$$E_i = \lambda_i / E \tag{9}$$

EXPERIMENTAL SET-UP AND PROCEDURE

The experiments were performed in a re-circulating open channel having a test section that was 2500 mm long, 200 mm wide and 200 mm deep. The side and bottom walls of the channel were made of clear acrylic to facilitate PIV measurement. The test model comprised a pair of two-dimensional acrylic circular cylinders, each with diameter, D = 12.7 mm. A digital Vernier caliper was used to measure the diameter, D of the cylinder at 30 randomly selected locations along the cylinder length, and it was found that $D = 12.2 \pm 0.15$ mm. A provisional test section made from 6 mm thick acrylic plate was inserted into the main channel to hold the cylinders. The insert was 2480 mm long, 184 mm wide and 194 mm deep, and its base was tightly screwed onto the floor of the main channel. The pair of cylinders was held perpendicularly to the side walls of the provisional test section and adjusted to selected vertical positions. Figure 1a shows schematic of a three-dimensional view of the inserted test section, the CCD camera and the laser arrangement while Figure 1b defines additional flow nomenclature and the coordinate system adopted. As shown, x, y, and z are, respectively, in the streamwise, transverse and spanwise directions; x = 0 is at the trailing edge of the cylinder which is located at 1250 mm; y = 0 is at the mid-point of the center-to-center distance between the cylinder pairs; z = 0 is at the channel mid-span, and y' is at the surface of the plane wall. The height h_l is the gap between the bottom surface of the lower cylinder and the plane wall (*i.e.* floor of the inserted test section) while h_u is the gap between the bottom surface of the upper cylinder and the plane wall.

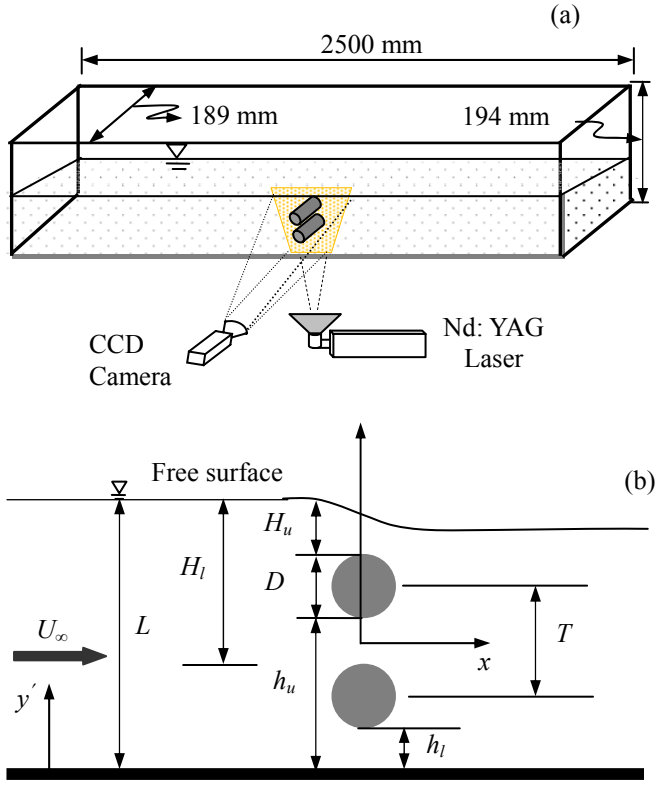

Figure 1: (a) a three-dimensional view of the inserted test section, the CCD camera, and the laser arrangement and (b) side view of the test section with the coordinate system and key geometrical parameters.

The submergence depth is defined as the gap between the cylinder upper surface and the free surface. Here, the height H_l is the gap between the upper surface of the lower cylinder and the free surface while H_u is the gap between the upper surface of the upper cylinder and the free surface. Measurements were performed for the following 3 test cases: Test 1: $h_{l,1}/D$ = 0.5 and $h_{u,1}/D$ = 2.5; Test 2: $h_{l,2}/D$ = 2.5 and $h_{u,2}/D$ = 4.5; and Test 3: $h_{l,3}/D$ = 4.5 and $h_{u,3}/D$ = 6.5. The pitch ratio, T/D for each of the test cases is 2. Test 2 will be used as the reference test case in discussing the effects of free surface and wall proximity. The approach freestream velocity (U_∞ = 0.3 m/s), Reynolds number (Re = 3810) and depth of flow (L = 101 ±1.5 mm) were maintained constant in all the experiments.

PIV SYSTEM AND DATA PROCESSING

A PIV technique was used to conduct the velocity measurements. The flow was seeded with 5 μm polyamide seeding particles having a specific gravity of 1.03. An Nd-YAG, 120 mJ/pulse laser of 532 nm wavelength was used to illuminate the flow field. The laser sheet was located at the mid-plane of the channel and perpendicular to the camera. A 12-bit high-resolution digital camera (Dantec Dynamic HiSense 4M camera) that uses a CCD with 2048 pixels × 2048 pixels and has a 7.4 μm pixel pitch was used to image the flow field. The measurements were made at field of view of 105 mm × 105 mm which corresponds to 8.3D × 8.3D in the streamwise and transverse directions of the flow. The instantaneous images were processed using the adaptive correlation option of FlowManager developed by Dantec Dynamics Inc. A three-point Gaussian curve fit was used to determine particle displacement with sub-pixel accuracy. An interrogation area of 32 pixels × 32 pixels with 50% overlap was employed. With this interrogation area size, the spacing between adjacent vectors is 0.92 mm or 0.07D. The particle image diameter was d_p = 2.1 pixels, which is very close to the recommended optimum value of $d_p \approx 2$ pixels required to minimize peak locking (Raffel et al. [15]). Based on preliminary convergence tests, 1200 instantaneous image pairs were used to compute the mean velocity and turbulence statistics reported subsequently.

Measurement uncertainty analysis was made following the AIAA standard derived and explained by Coleman and Steele [16]. The guidelines and steps necessary to minimize the bias and precision errors in PIV measurements are discussed by Prasad et al. [17] and Forliti et al. [18]. In this study, the uncertainties in the mean velocities and Reynolds shear stresses at 95% confidence level were estimated to be ±2% and ±10%, respectively, of the corresponding maximum values.

FLOW QUALIFICATION

Velocity measurements were obtained at x/D = -25 (i.e., upstream of the cylinders) to characterize the approach flow.

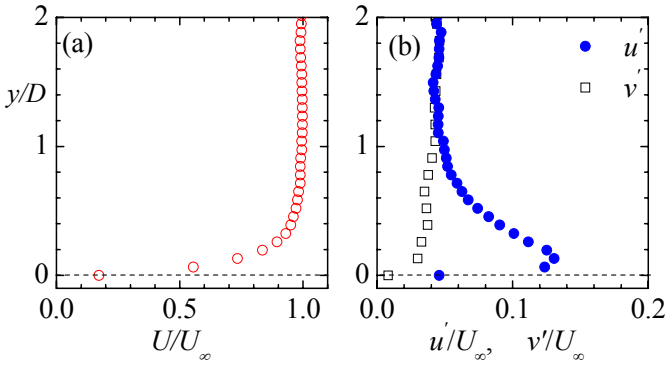

Figure 2: Profile of: (a) streamwise mean velocity and (b) streamwise and transverse components turbulence intensity.

As stated earlier, the approach freestream velocity and depth of flow were maintained at U_∞ = 0.3 m/s and L = 101 mm, respectively. The corresponding Reynolds number based on the approach velocity and depth of flow ($Re_L = U_\infty L/\nu$) was 30300 while the Froude number ($F = U_\infty /[gL]^{0.5}$) was 0.3. The approach flow was, therefore, in turbulent and sub-critical regimes.

The mean streamwise velocity distribution is shown in Figure 2a while the turbulence intensities are shown in Figure 2b. The profiles are as expected for an open channel flow. The background turbulence level close to the free surface was u/U_∞ = 0.05, which is an order of magnitude higher than typical values reported in wind tunnel experiments.

RESULTS AND DISCUSSION

Iso-contours of mean velocity and turbulence kinetic energy

The iso-contours of the mean streamwise velocity (U) and turbulence kinetic energy (k) for all test cases are shown in Figure 3. The kinetic energy was approximated from $k = 0.5(u^2 + v^2)$ where u and v are, respectively turbulent intensities in the streamwise and transverse directions. The iso-contours were made dimensionless using the approach velocity (U_∞). The corresponding mean streamlines are superimposed on each plot to reveal the mean flow pattern. The approximate locations of the cylinders are also shown. As expected, the iso-contour of U for each test case reveals a pair of counter rotating vortices behind each cylinder, however, the stagnation point, position of separation, and vortex formation show significant dependence on the depth of submergence of the cylinder pairs. Figure 3a shows that the size of the recirculation bubbles behind the upper cylinder is significantly smaller than those of the corresponding lower cylinder. It is apparent that the recirculation bubbles behind the cylinder pairs declined downwards, which is due to a jet-like flow formed in the gap region between the upper cylinder and the free surface. The active mixing with the jet-like flow causes the ambient fluid to be entrained into the wake and invariably causes a reverse flow in the region near the free surface. It is noted that the degree of declination of the recirculation bubbles in lower cylinder is less step compared to the upper cylinder. This observation is consistent with the findings of Daichin and Lee [6] on flow past a single circular cylinder adjacent to a free surface. For Test 2 (Figure 3b), the vortices are nearly similar in size and also symmetrical about the wake axis. This behavior closely represents that of an isolated circular cylinder in a uniform flow. It is observed that the recirculation zone behind the lower cylinder is relatively narrower than those found behind the upper cylinder. It appears that the flow is biased towards the lower cylinder thereby making the vortices behind it smaller in size. Sumner et al. [7] reported a similar observation. The proximity of the lower cylinder to the plane wall adds to the complexity of the flow as it tends to channel the approach flow

between its upper surface and the wall. This causes the fluid to accelerate in the narrow gap as evident by high velocity in Figure 3c. This feature is absent from the cylinder pairs in a uniform flow (Figure 3b). It appears that the lower vortex is dominating and tends to diffuse the upper vortex.

High magnitudes of turbulence kinetic energy are evident in regions of recirculation bubbles, and along the sides of the cylinders (Figures 3d - 3f). Moreover, the value of k is relatively higher for the cylinder pairs in Test 1, especially for the upper cylinder.

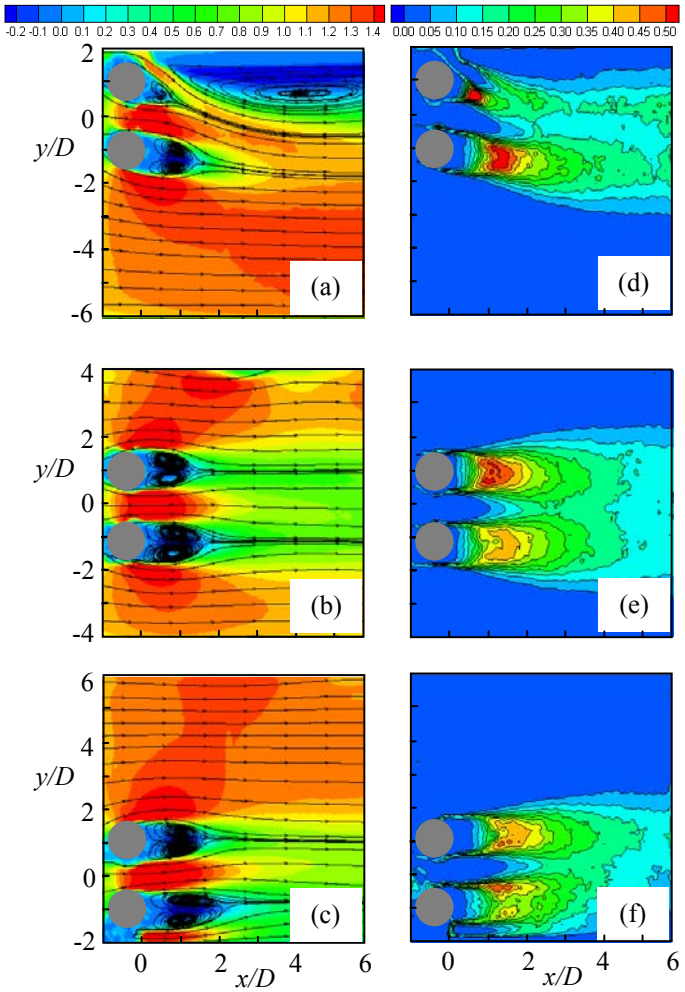

Figure 3: Contours of mean streamwise velocity (U/U_∞) and streamlines: (a), (b), and (c) are, respectively for Test1, Test2, and Test3; correspondingly, contours of turbulence kinetic energy (k/U_∞^2): (d), (e), and (f).

Mean velocity along the wake

It is important to note that the line $y = 0$ is equidistant of the spacing between the cylinder pairs, while a wake axis refers to a streamwise line through the centre of a cylinder. The distribution of the mean streamwise velocity along the wake axis can provide useful insight into the downstream evolution of the wake. For example, the streamwise mean velocity shown in Figure 4 would provide information about the length of the recirculation, L_r, as well as recovery of the mean flow towards the approach flow (*i.e.* $U/U_\infty = 1$). The length of recirculation is defined as the distance between the cylinder trailing edge and the downstream location where the streamwise mean velocity becomes zero. In these and subsequent plots, appropriate intermediate data points are skipped for clarity. Figures 4a shows that nearness to free surface and wall proximity have significant effect on $(U/U_\infty)_{min}$ and L_r/D. For all test cases, the magnitude of U/U_∞ initially decreases with distance along the wake axis with $(U/U_\infty)_{min}$ occurring at about the middle of L_r and then start to increase thereafter. The values of $(U/U_\infty)_{min}$ are approximately -0.11, -0.26 and -0.30, respectively, for Tests 1, 2 and 3 (Figure 4a). For the lower cylinder (Figure 4b), the values of $(U/U_\infty)_{min} \approx$ -0.34 for Test 1, -0.28 for Test 2, and -0.34 for Test 3. Meanwhile, the values of $L_r/D \approx$ 1.37, 1.70 and 2.0 respectively, for Test 1, Test 2, and Test 3 in Figure 4b are longer than the corresponding values obtained for the upper cylinders (Figure 4a). The subsequent recovery of the mean flow in the very near-wake region is fastest for Test 1 and slowest for Test 3. This implies that the close proximity of the plane wall increases the recirculation length and slows down the recovery, while nearness to free surface decreases the recirculation length and hastens the recovery.

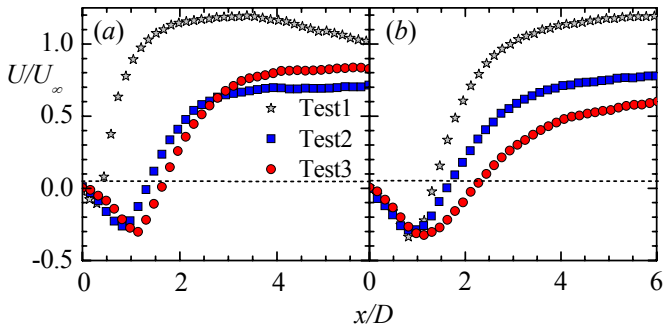

Figure 4: Mean velocity along the wake centerline: (a) upper and (b) lower cylinders.

Production of turbulence kinetic energy

The full transport equations for the Reynolds stresses and turbulence kinetic energy can be found in Hinze [19]. For a two-dimensional turbulent flow, the production terms in u^2, v^2 and uv are, respectively, $P_{uu} = [-u^2\partial U/\partial x - uv\partial U/\partial y]$, $P_{vv} = [-v^2\partial V/\partial y - uv\partial V/\partial x]$ and $P_{uv} = [-uv(\partial U/\partial x + \partial V/\partial y)] - [u^2\partial V/\partial x - v^2\partial U/\partial y]$. Similarly, the production term in the turbulent kinetic energy equation is $P_k = [-uv(\partial U/\partial y + \partial V/\partial x)] - [u^2\partial U/\partial x + v^2\partial V/\partial y]$. For P_k, the first two terms on the right hand side consists of contribution from normal stresses ($P_{k,N}$), while the last two terms from shear stresses ($P_{k,S}$). The production terms above were estimated directly from measured data. It was found that $\partial U/\partial y >> \partial V/\partial x$ and $\partial U/\partial x \approx -\partial V/\partial y$ so that P_k is well approximated by $-uv\partial U/\partial y$ and P_{uv} by $-v^2\partial U/\partial y$. Here, P_{uu}

$\approx P_k$ while P_{vv} is negligible. It is recognized that the magnitude of each term in $P_{k,N}$ is individually high, however, their sum is smaller than the individual terms because they are of opposite signs. The distribution of P_k and P_{uv} at $x/D = 2$ are, respectively shown in Figures 5a and 5b. As expected, Figure 5a shows a trend similar to that of Reynolds shear stress ($-uv$) with double peaks of approximately -0.3 and 0.3 for Test 1 and -0.4 and 0.4 for Test 3. On the other hand, P_{uv} (Figure 5b) shows a trend similar to the turbulence kinetic energy, k with double positive peaks. The magnitudes of the peaks are larger for Test 3 and least for Test 1. These trends show that irrespective of the location of cylinder pairs, the magnitudes of P_k are generally higher than those of P_{uv}.

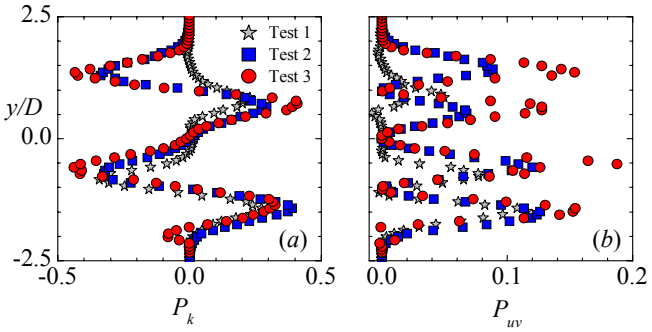

Figure 5: Profiles of normalized dominant terms in the transport equations for: (a) turbulence kinetic energy {$P_k = -uv\partial U/\partial y(D/U_\infty^2)$} and (b) Reynolds shear stress {$P_{uv} = -v^2\partial U/\partial y(D/U_\infty^2)$}.

RESULTS OF POD ANALYSIS

Convergence Test and Energy Spectra

The convergence of the POD is defined as the ratio of the energy contained in the ith mode to the total turbulent energy in the flow field (i.e., the contribution of each mode to the total kinetic energy). Moreover, the number of snapshots required to adequately capture the energy content of a given mode depends largely on the nature or complexity of the flow. Following previous studies, the fractional contributions of the first two eigenvalues (λ_1^* and λ_2^*) with increasing number of snapshots were calculated. The results for the three test cases are summarized in Table 1. It is observed that the variation of λ_1^* and λ_2^* with N is less than ±0.4% for $N \geq 800$. Consequently, the POD analysis based on 1200 snapshots used in the present study is sufficient to achieve converge results. The number of snapshots used in the present study is higher than $N = 500$ used to analyze the near-wake region of a square cylinder at incidence by van Oudheusden et al. [20]. In general,

Table 1: Summary of energy convergence test using the first two POD modes for Tests 1, 2, and 3.

Snap -shot (N)	Test 1		Test 2		Test 3	
	$\lambda^*_n = \lambda_n/\Sigma\lambda_n$ (%)		$\lambda^*_n = \lambda_n/\Sigma\lambda_n$ (%)		$\lambda^*_n = \lambda_n/\Sigma\lambda_n$ (%)	
	λ^*_1	λ^*_2	λ^*_1	λ^*_2	λ^*_1	λ^*_2
200	9.6	8.7	10.0	9.4	9.8	8.6
400	8.9	8.5	10.5	8.6	9.7	8.6
600	8.9	8.4	9.9	9.0	9.3	8.8
800	8.7	8.5	9.6	8.7	9.0	8.8
1000	8.8	8.3	9.3	8.8	8.9	8.5
1200	8.7	8.2	9.1	8.9	8.9	8.3
1400	8.6	8.1	9.1	8.8	8.7	8.3
1600	8.5	8.1	9.1	8.6	8.6	8.3

The cumulative and fractional contributions of the POD modes to the turbulence kinetic energy for all test cases are plotted in Figure 6, to illustrate the effectiveness of the POD to capture energy in the near wake. The cumulative turbulence energy distribution (Figure 6a) increases rapidly at lower modes and then slowly converges with increasing modes thereafter for Test 1, Test 2, and Test 3. The dramatic increase indicates that the lower modes contain most of the turbulence energy while the higher have smaller scale flow structures. Figure 6b reveals that for $i \geq 4$, the energy associated with the modes decrease very rapidly with increasing mode. For example, the modal energy contribution drops more than an order of magnitude from approximately 8.7%, 9.1%, and 8.9%, respectively for Test 1, Test 2, and Test 3 in the first 30 modes, suggesting that most of the turbulence kinetic energy resides in the first few modes.

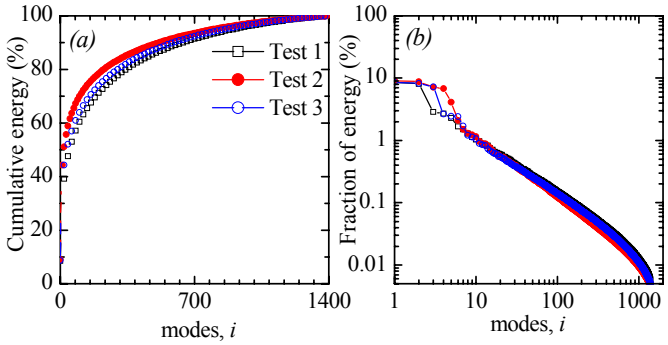

Figure 6: Spectra of turbulent kinetic energy: (a) accumulated turbulent kinetic energy ratio of modes as a function of mode number (b) fractional contribution to the turbulent kinetic energy by the modes.

Comparisons of the magnitudes of the first two most energetic modes for all test cases reveal a variation in magnitude of less than 5%. However, the magnitudes of modes 1 and 2 for Test 2 are slightly larger than the corresponding values for Test 1 and Test 3. It can be inferred that the turbulence kinetic energy shows no significant dependence on depth of submergence in the near wake of cylinder pairs.

Reconstruction of the Turbulence Quantities

Low order representations of the instantaneous velocity fields for all test cases were reconstructed from the first n = 1, 5, 20, and 50 POD modes. From the reconstructed velocity fields, the profiles of the corresponding turbulence intensities and Reynolds shear stresses were obtained and used to quantitatively illustrate the cumulative effect of low order modes in the data reconstruction. This was done by comparing the reconstructed profiles at x/D = 2 with the corresponding profiles obtained from the ensemble PIV data. Figures 7 and 8 show that as the number of the modes is increased, a consistent progression towards the profiles of the PIV data is observed. As expected the quantities converge faster outside the wake region.

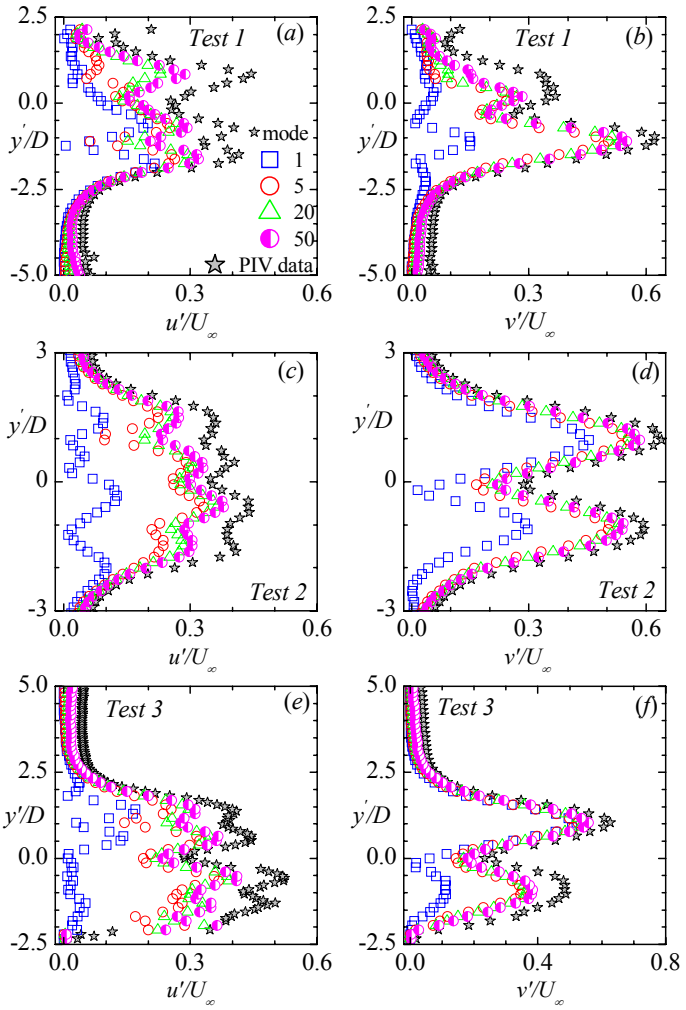

Figure 7: Profiles of reconstructed turbulence quantities from the first 1, 5, 20, and 50 modes across the wake at *x/D* = 2. Note: PIV data are the ensemble averaged.

It is observed that for all test cases, the profiles of the Reynolds shear stresses approach the PIV data faster than the turbulence intensities, while the recovery of the streamwise turbulence intensity is slowest. It can be inferred from this result that large scale coherent structures would play significant dynamic roles in the Reynolds shear stress and transverse component of turbulence intensity than for the streamwise component.

It should also be noted that the values of v are generally larger than those of u for all test cases, signifying larger contribution from v to turbulent kinetic energy. For all the quantities, recovery is generally faster in the upper half than the lower half due to the complexity of the flow in the vicinity of the plane wall and free surface.

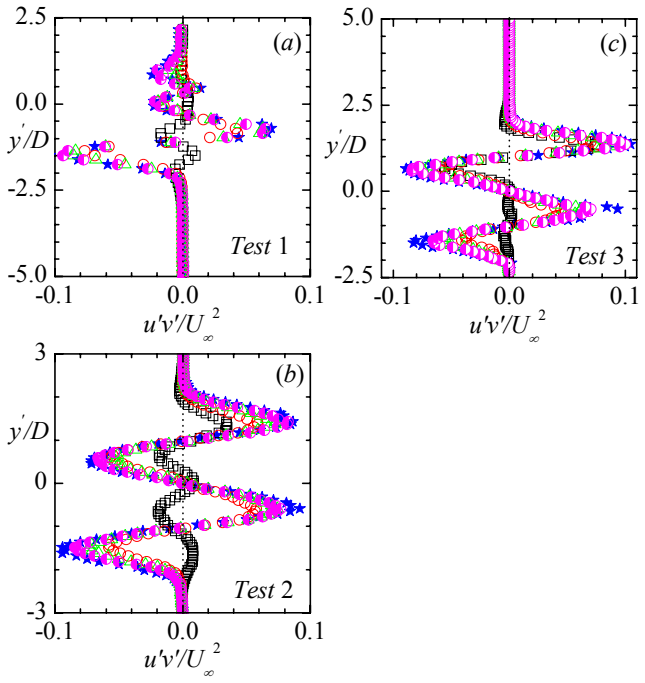

Figure 8: Profiles of reconstructed Reynolds shear stress from the first 1, 5, 20, and 500 modes across the wake at *x/D* = 2. Symbols are same as in Figure 7.

CONCLUSIONS

In the present study, a combination of PIV and POD analysis were employed to investigate flow around and in the near-wake of a pair of circular cylinders. Measurements were conducted at three different depths of cylinders submergence and the flow structures analyzed. The results show that the close proximity of the plane wall increases the recirculation length and slows down the recovery, while nearness to free surface decreases the recirculation length and hastens recovery. Irrespective of the location of the cylinder pairs, the magnitude of turbulence production by the kinetic energy is generally higher than those of Reynolds shear stress. Moreover, as the number of POD modes increased, the reconstructed turbulence intensities and Reynolds shear stress show that the large scale structures contribute most to Reynolds shear stress and least to streamwise turbulent intensity.

ACKNOWLEDGMENTS

The author gratefully acknowledges Dr. Mark Tachie for the use of his Lab. facilities which were founded through a grant by Canada Foundation for Innovation (CFI) and Natural Sciences & Engineering Research Council of Canada (NSERC) Discovery Grant.

REFERENCES

[1] Price, S.J., Sumner, D., Smith, J.G., Leong, K., and Paidoussis, M.P., 2002, "Flow visualization around a circular cylinder near to a plane wall," *J. Fluids and Structures*, 16 (2), pp., 175-191.

[2] Bearman, P. W. and Zdravkovich, M. M., 1978, "Flow around a circular cylinder near a plane boundary," *J. Fluid Mech*., 89, pp. 33-47.

[3] Dipankar, A. and Sengupta, T. K., 2005, "Flow past a circular cylinder in the vicinity of a plane wall," *J. Fluids and Structures*, 20, pp. 403-423.

[4] Sheridan, J., Hourigan, K., and Thompson, M. C., 1996, "Flow past a cylinder close to a free surface," *J. Fluid Mech*., 330, pp. 1-30.

[5] Reichl, P. and Lin, J. C., and Rockwell, D., 2007, "Flow past a cylinder close to a free surface," *J. Fluid Mech*., 533, pp. 269-296.

[6] Lee, S.J. and Daichin, 2004, "Flow past a circular cylinder over a free surface: Interaction between the near wake and free surface deformation," *J .Fluids and Structures*, 20, pp. 403-423.

[7] Sumner, D., Wong, S.S.T., Price, S. J., and Paidoussis, M. P., 1999, "Fluid behaviour of side-by-side circular cylinders in steady cross-flow," Journal of Fluid Strut*.,* 13, pp.309–338.

[8] Wang, Z. J. and Zhou, Y., 2004, "Vortex interactions in a two side-by-side cylinder near-wake", *Int. J. Heat and Fluid Flow,* 26, pp. 362 – 377.

[9] Lumley, J. L, 1967, "The Structure of Inhomogeneous Turbulence," *Atmospheric Turbulence and Wave Propagation* ed. Yaglon, A. M. and Tatarski, V. I., Nauka, Moscow, pp. 166-178.

[10] Hammad, K, and Milanovicc, I., 2009, "A POD Study of an Impinging Jet Flow,

[11] Berkooz, G., Holmes, P., and Lumley, J. L., 1993, "The Proper Orthogonal Decomposition in the Analysis of Turbulent Flows," *Ann. Rev. Fluid Mech*., pp. 25, 539 – 575.

[12] Holmes, P., Lumley, J. L., and Berkooz G., 1998, "Turbulence, Coherent Structures, Dynamical Systems and Symmetry," Cambridge University Press.

[13] Delville, J., 1994,"Characterization of the Organization of in Shear Layer via the Proper Orthogonal Decomposition," *Applied Science Research*, 53, pp. 263 – 281.

[14] Sirovich, L., 1987, "Turbulence and the dynamics of coherent structures," Part 1: Coherent structures, *Quarterly J. App. Math*, 45, (3), pp. 561 – 571.

[15] Raffel, M., Willert, C.E., and Kompenhaus, J., 1998, "Particle Image Velocimetry: A Practical Guide," New York, Springer.

[16] Coleman, H.W. and Steele, W.G., 1995, "engineering application of experimental uncertainty analysis," *AIAA J*., 33, pp., 1888-1896.

[17] Prasad, A. K., Adrian, R. J., Landreth, C.C. and Offutt P. W., 1992, Effect of resolution on the speed and accuracy of particle image velocimetry interrogation," *Exp. Fluids*, l3, pp., 105-116.

[18] Forliti, D. J., Strykowski, P. J., and Debatin, K., 2000, "Bias and precision of digital particle image Velocimetry," *Exp. Fluids*, 28, pp. 436-447.

[19] Hinze, J. O., 1975, "Turbulence," McGraw-Hill, New York.

[20] van Oudheusden, B. W., Scarano, F., van Hinsberg, N. P., and Watt, D. W., 2005, "Phase-Resolved Characterization of Vortex Shedding in the Near Wake of a Square-Section Cylinder at Incidence," *Expt. Fluids*, 39, pp. 86-98.